Acta Materialia 285 (2025) 120659

Contents lists available at ScienceDirect

Acta Materialia

journal homepage: www.elsevier.com/locate/actamat

Plastic flow in Fe-Cr-Ni austenitic steel under the presence of solute H: A study via room temperature creep

Yuhei Ogawa *, Akinobu Shibata

Research Center for Structural Materials, National Institute for Materials Science (NIMS), 1-2-1 Sengen, Tsukuba, 305-0047, Japan

ARTICLE INFO

Keywords:
Austenitic steels
Hydrogen
Dislocations
Thermally activated deformation
Creep

ABSTRACT

A connection between the effects of solute hydrogen (H) on macroscopic flow stress and microscopic dislocation mobility has been a subject for understanding the plastic flow behavior of H-charged austenitic steels and other face-centered cubic (FCC) alloys. In this study, we try to solve this problem by examining the room temperature creep of a Fe-24Cr-19Ni-based Type310S austenitic stainless steel uniformly charged with 9000 at ppm solute H in a pressurized gaseous H_2 environment. Stress-dip test to decompose the flow stress into effective (thermal) and internal (athermal) stresses, as well as a brief analysis of dislocation structure development in deformed uncharged and H-charged samples by electron channeling contrast imaging and hardness measurement, were supplementally employed. It is emphasized that solute H atoms consistently act as short-range obstacles hindering the movement of dislocations and thereby causes significant solid solution-hardening. Nevertheless, two opposite H-effects to accelerate and retard the creep rate were macroscopically identified depending on whether the stress level applied to H-charged specimens is above or below the flow stress under non-charged condition. These newly found, seemingly contradicting phenomena were interpreted based on the stress-dependent change of the rate-controlling mechanisms predominating thermally activated dislocation motion. Primary rate-controlling obstacles are H atoms themselves when creep acceleration manifests at high stress, while H atoms, other alloying elements, and forest dislocations cooperatively work to retard creep under low stress. The potential model of dislocation motion under the presence of these multiple obstacle types is finally proposed.

1. Introduction

The flow stress in the plastic deformation of most engineering alloys exhibits its dependencies on temperature and time (*i.e.*, strain rate). These dependencies have their roots in the glide resistance of crystal dislocations to overcome the arrays of multiple obstacle kinds on the slip plane, a process aided by thermal vibration: *thermally activated motion* [1–3]. Under a given temperature, thermally activated dislocation motion is evidenced by stress relaxation and creep, *i.e.*, sluggish stress-decrease and strain-increase with the time elapsed after strain- and stress-holding, respectively [4,5]. In addition to their practical importance, these deformation transients have widely been used in the studies of rate-controlling mechanisms and obstacle types predominating the plastic deformation in various metallic materials [2,6–12].

The obstacles governing thermally activated dislocation motion have a short-range nature with an extent of only a few interatomic distances [2,3]. In well-annealed alloys with face-centered cubic (FCC) crystal structure, typical short-range obstacles are interstitial/substitutional solute atoms, a contribution of which is to cause solid solution-hardening in terms of flow stress [10,13–16]. Because of their significance in alloy design, the roles of two interstitial elements, carbon, C, and nitrogen, N, on temperature- and strain rate-dependent deformation, as well as on flow stress, have been established in FCC alloys and austenitic steels [16–21]. The local isotropic lattice expansion around these interstitials [20,22] retards the movement of dislocations when dislocations pass through their neighbor or dynamically pinning dislocations when the deformation temperature is high enough for interstitial diffusion [17–19,23]. Meanwhile, understanding the impact of another representative interstitial for engineering alloys, *i.e.*, hydrogen (H), remains elusive and incomplete. A reason for this lack of understanding is a much more complicated situation for H than C and N owing to its tiny atomic size. Indeed, solute H causes only minor lattice dilatation [24–26] and exhibits high diffusivity even around room temperature [27,28].

Since the 1960s, there has been an ever-continuing debate on whether solute H impedes or accelerates thermally activated movement

* Corresponding author.
E-mail address: OGAWA.Yuhei@nims.go.jp (Y. Ogawa).

https://doi.org/10.1016/j.actamat.2024.120659
Received 1 August 2024; Received in revised form 7 November 2024; Accepted 14 December 2024
Available online 16 December 2024

of dislocations in FCC metals and alloys [9,29–36]. Although macroscopic strengthening (*i.e.*, increases in flow stress and indentation hardness) or serrated yielding after H-charging was reported in pure Ni [32,37–41], Ni-alloys [33,37,42], FCC high entropy alloys [34,43], and austenitic steels [35,36,44–46], a conflicting phenomenon was identified by *in-situ* tensile experiments in an environmental transmission electron microscope (TEM) that H conversely enhances dislocation mobility [29,47,48]. Introduction of H_2 gas in TEM chamber increased the velocity of dislocations [29,49], besides decreases the equilibrium distance between dislocations piling-up against grain boundary under a given applied stress/strain [47]. These findings in TEM has been believed to be an intrinsic effect of diffusible H atmosphere that dynamically interacts with moving dislocations, wherein the dislocation's interaction with surrounding obstacles can somehow be weakened [29]. However, recent dedicated studies using atomistic simulations pose a question about such a specific phenomenon confirmed in the TEM approach [50,51]. The macroscopic strengthening in the H-containing FCC metals and alloys has sometimes been ascribed to the impact of H on the development process of dislocation structures [42,52,53] or H-induced propensity for the deformation heterogeneity within localized slip bands [31,54–57]. Nevertheless, recent dedicated study on single crystalline Type316L steel having various crystallographic tensile orientations clarified merely subtle H-impact on their work-hardening characteristics [58]. This last fact infers that the strengthening has its root on the influence of H on the glide resistance of individual dislocations rather than any effects on collective dislocation behaviors particularly in Fe-based austenitic materials.

Amongst this long-standing uncertainty, the authors' systematic stress relaxation studies have substantiated the dislocation-impeding effect of solute H, particularly in a Type310S austenitic stainless steel [59,60]. Our series of experiments successfully indicated that solute H could act as short-range obstacles for moving dislocations, increasing matrix frictional resistance similarly to other conventional alloying elements. Notably, the authors' conclusion aligns well with the latest crystal plasticity modelling works, where H-induced increase in dislocation glide activation energy or drag resistance by H-atmosphere were incorporated to reproduce the experimentally obtained stress-strain curves [61,62]. Besides, an enhancement of H-induced solid solution-hardening by increasing the strain rate also supports thermally activatable character of the obstacle H atoms for dislocations [34]. This paper is a continuation of our previous works, aiming to establish further proof of our statement and build up a new glide process model of dislocations in a combined field of solute H and other intrinsic obstacles (*i.e.*, alloying elements and forest dislocations). The experimental approach is extended to creep deformation in the same alloy, which is associated with thermally activated dislocation motion under the influence of solute H.

Considerable creep strain can be observed in austenitic steels even at relatively low temperatures (*e.g.*, < 400 K) [63–65]. Relying on this material property, Tien and Altstetter evaluated the effect of cathodically charged H on the magnitude and rate of transient creep in a thin sheet (~30 μm thickness) of Type310S stainless steel at 328 K [30]. Thanks to their efforts, it has been demonstrated that solute H with 15,000~47,000 at ppm slowed down the initial creep rate within a short time (~30 s), while the deformation sluggishly continued over a longer time (~50,000 s) in the H-charged sample. They ascribed the latter fact to an increasing mobility of dislocations due to the presence of H [29,47,48]. Nevertheless, despite the identified longer creep duration, the total creep strain in the H-charged specimen was, in most situations, smaller than that in the non-charged case [30]. Given that the H-induced dislocation-impeding effect found by the present authors [59,60] is a universal phenomenon, such a slowly continuing but lesser magnitude plasticity can also be viewed as a retardation of creep, where dislocation movement is simply delayed due to the presence of newly involved obstacles: H. On the other hand, in the nano-indentation experiment under a fixed load, Hong et al. recently exhibited clear evidence of an increased total creep strain in a Type310S steel after H-charging in a pressurized H_2 gas [66]. For the progress of our understanding beyond these variable past discoveries, one requires a more refined experimental framework that provides a holistic view of the macroscale creep behavior in H-containing austenitic steels and its interrelation with the H-induced change in the latent dislocation mobility.

The present study deals with the room temperature creep of a Type310S austenitic steel uniformly charged with 9000 at ppm H under systematically controlled stress-strain setups. A primary advantage of adopting creep experiment is that it provides plastic deformation properties under fixed stress, while stress relaxation [59,60] involves a continuous decrease in the driving force for deformation. Such simplicity enables us to get more straightforward pictures regarding the underlying deformation mechanisms. We found both apparent and intrinsic H-effects in accelerating and retarding creep deformation, which shows their consistent stress-dependence as clarified by a comparative evaluation with a monotonic tensile flow curve. The function of solute H was further elaborated by decomposing the flow stress into effective and internal stresses, as well as by measuring activation volume as a parameter reflecting predominant rate-controlling mechanisms. These overall characteristics were thoroughly interpreted based on the concept that H atoms no less act as thermally activatable obstacles for dislocations.

2. Methodology

2.1. Material and specimen

A φ20 mm rod of Type310S steel with the composition of Fe-24.17Cr-19.11Ni-1.11Mn-0.28Si-0.02C-0.031P-0.001S (mass%) was used. The final solution treatment was carried out at 1353 K for 10 min, followed by water quenching. Fig. 1(a) shows the initial microstructure on the section perpendicular to the rod axis, captured by electron backscattered diffraction (EBSD) in a scanning electron microscope (SEM), Zeiss SIGMA. The material has randomly oriented equiaxed grains with an average grain diameter of 50 μm excluding annealing twins. Cylindrical tensile specimens with a diameter of 4 mm and a parallel part length of 30 mm (Fig. 1(b)) were machined from the rod center, the surfaces of which were mirror-finished by 1 μm diamond suspension.

2.2. Charging method and concentration of hydrogen

H-charging was conducted prior to the mechanical tests by exposing the specimens to H_2 gas environment at 100 MPa and 543 K for 200 h in an autoclave. Considering the H diffusivity in Type310S steel at 543 K (*e.g.*, 1.0×10^{-11} m^2/s [67]), these charging temperature and time are sufficient to achieve a uniform H distribution within the specimen's gauge part [36,68,69]. After the mechanical tests, some cylindrical samples with 4 mm length were cut from the specimens subjected to creep and stress-dip tests (cf. Section 2.3), the residual H concentration of which was measured by thermal desorption spectroscopy (TDS). The TDS was conducted by a quadrupole mass spectrometer (HTDS-004, R-DEC, Japan) with a heating rate of 200 K/h and a maximum temperature of 1073 K. Fig. 1(c) shows the representative H desorption profiles during the TDS. The H concentration was 200 at ppm (4 mass ppm) for the non-charged specimen and 9000 at ppm (166 mass ppm) for the H-charged specimen.

In order to confirm that the observed changes in the flow behavior truly stem from the pure effect of solute H, some non-charged specimens were heat-treated in air (543 K for 200 h) and mechanically tested as well.

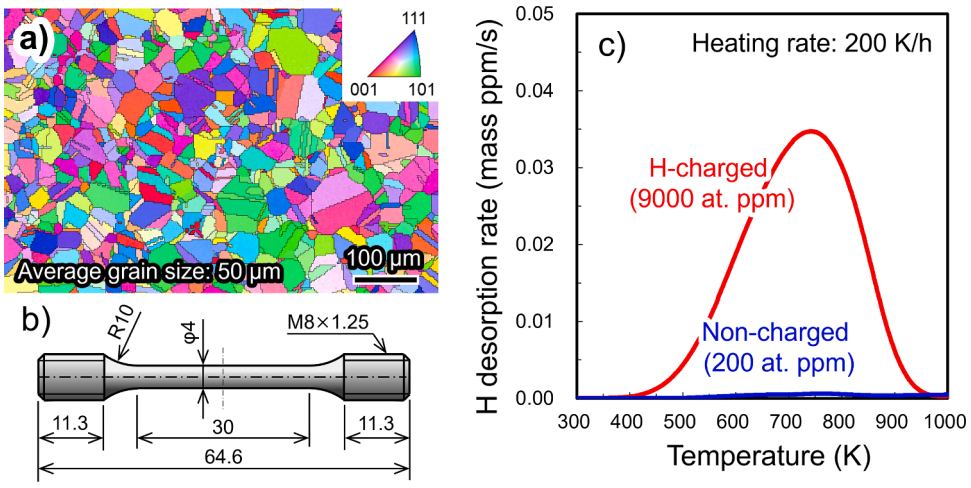

Fig. 1. (a) Microstructure of the Type310S steel on the plane normal to the rod axis. The image was captured by electron backscattered diffraction (EBSD). The shape and dimensions of the cylindrical specimen are depicted in (b), while H desorption profiles from H-charged and non-charged specimens in the TDS measurements are shown in (c).

2.3. Mechanical tests

2.3.1. Stepwise creep tests

The creep behaviors of H-charged and non-charged specimens were evaluated at multiple stress and strain levels by implementing 1000 s load holdings on the way of tensile deformation (Fig. 2(a)). All the tests were performed by a screw-driven electromechanical test frame with a 20 kN load capacity (Shimadzu, AGX-V2) at the temperature of 295±1 K. The tensile straining was imposed with a constant crosshead speed of 0.003 mm/s (initial strain rate of 1×10^{-4}/s), followed by an immediate change in the controlling mode to a constant load when the stress/strain reached the targeted values. A contact-type strain gauge extensometer with a 25 mm gauge length was attached to the specimen's gauge part for the strain measurement during the tensile deformation and creep. The creep strain in this study was defined as the displacement of the extensometer during creep, which is divided by the original distance between the edges of the extensometer at the start of each creep phase. Nonetheless, the creep strain was sometimes too small (*e.g.*, < 0.01 %) to be measured accurately, where electronic noises drowned out the extensometer's signal. In such a case, the creep strain was approximated as the machine crosshead displacement divided by the nominal length of the specimen's parallel part (*e.g.*, when the applied nominal strain before creep was 10 %, the parallel part length of 33 mm was used for the calculation). As per the references, normal monotonic tensile tests without intermediate load holdings were also carried out.

2.3.2. Creep tests with pre-straining or stress-dip

Because of the flow stress increase by solute H, the total strain at the start of creep under a given stress is lower for the H-charged specimen than for the non-charged specimen. In turn, the starting stress for creep is higher for the H-charged specimen under a fixed strain. These discrepancies of strain or stress make the interpretation not straightforward since the creep behavior is synergistically affected by applied stress and strain [63,64,70,71]. To solve this issue, two types of additional tests involving pre-straining or prompt stress-dip were performed.

In the first test (Fig. 2(b)), H-charged and non-charged specimens were pre-strained to 10 % nominal strain and rapidly unloaded. Then, the specimen diameter was re-measured. Stress was successively applied, and held for 1000 s. The critical stress at which creep deformation starts was detected, in addition to recording the creep strain.

In the second test (Fig. 2(c)), the H-charged specimen was monotonically deformed to a targeted strain. Subsequently, rapid partial unloading to the level equivalent to the flow stress in a non-charged specimen, $\sigma_{f,non}$, was implemented, followed by 1000 s load holding. This procedure was repeated at several different strains. The essence of these experiments is to unify both the strain and stress at the start of creep for H-charged and non-charged specimens. Hence, the tests in Section 2.3.1 provide an apparent H-effect on creep, whereas those in this section try to extract the true influence of H.

2.3.3. Decomposition of flow stress

Besides the stress component stemming from thermally activated dislocation motion, there exist other contributions to flow stress that are independent of temperature and strain rate [2,3,72]. These extra stress components are called internal or athermal stress, σ_i, in contrast to the effective stress, σ_{eff}, rooted in short-range obstacles (Section 1). σ_i is

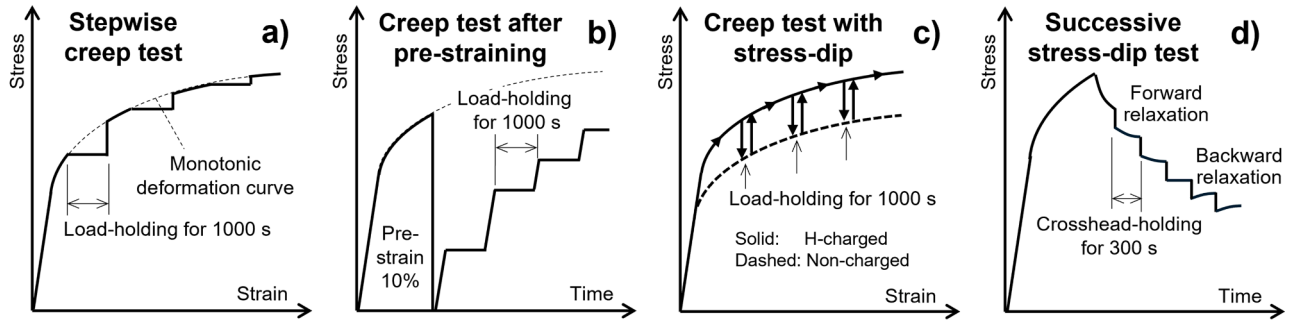

Fig. 2. Schematics of the test procedures implemented in this study. (a) Stepwise creep test, (b) Creep test with pre-strained specimen, (c) Creep test with partial unloading, and (d) Successive stress-dip test for the decomposition of stress components.

further subdivided into non-polarized and polarized components. The origin of the former may be an energy required to break away attractive junctions between mobile and forest dislocations [73–75]. On the other hand, the latter component is caused by long-range repulsive interactions between pile-up dislocation groups or the development of intragranular-scale heterogeneities in dislocation structures [76–78]. This polarized stress component is also designated as back stress, σ_x, accounting for a major part of σ_i in the case of FCC alloys [78]. Distinguishing the contributions from these individual stress components may give us additional insights into the roles of H on creep deformation.

Several methods have been proposed for decomposing these stress components using stress relaxation or stress-reduction techniques [72, 79–81]. Here, we employed MacEwen's method [80], wherein stress-dip and subsequent strain-holding are successively implemented (Fig. 2(d)). When the applied stress is larger than σ_i and still includes σ_{eff} component, this effective stress is relaxed *via* the forward movement of dislocations (*i.e.*, movement in the same direction during the tensile straining) with the aid of time. Under such circumstances, the material exhibits a stress decrease under a fixed strain (forward relaxation). Meanwhile, the relaxation ceases, and the direction of time-dependent stress transition is eventually reverted due to the backward motion of dislocations once the applied stress falls below σ_x (backward relaxation). Such behavior has been well-known as the Bauschinger effect [76,77]. Thus, finding the point at which relaxation changes from forward to backward (or becomes zero) enables us to roughly distinguish the contributions from σ_{eff} and σ_i (σ_x) to the total flow stress.

In the present study, the successive stress-dip was performed by a step of 5 MPa nominal stress, followed by 300 s holding of the machine crosshead. This successive stress-dip was implemented at several strain levels during the tensile deformation. Note that the stress resolution in our experimental set-up was better than 0.02 MPa.

2.4. Microstructural analysis

For a proper interpretation of the H-effects on creep, it is also essential to know the significance of H-impacts on the development of dislocation structures. Thus, dislocation structures in non-charged and H-charged specimens monotonically deformed to 10 % nominal strain (*i.e.*, intermediate strain level in the present study) with a strain rate of 1×10^{-4}/s were analyzed by electron channeling contrast imaging (ECCI) in an SEM. The observations were carried out with two-beam diffraction conditions in a Zeiss SIGMA SEM operated at 25 kV. The samples with their planes parallel to the tensile axis were cut from the deformed specimens, the surfaces of which were polished by colloidal SiO_2 suspension (Struers, OP-S). The crystal orientations of the observed grains were analyzed separately by EBSD (Bruker QUANTAX system).

Vickers hardness, *HV*, of deformed samples were measured for a more statistical significance on the magnitude of the development of deformation microstructure than local SEM analysis. 1.5 mm-thick disks were prepared from the non-charged and H-charged specimens deformed to 10 % nominal strain, and some of them were annealed at 500 K for 120 h to desorb H, *i.e.*, to eliminate the effect of solute H themselves (*i.e.*, solid solution-hardening) on the hardness. The *HV* was determined as an average of 20 points measurements with an indentation load of 9.8 N and a holding time of 30 s.

3. Results

3.1. Flow and creep behavior during monotonic deformation

The nominal stress, σ_N, versus nominal strain, ε_N, curves of non-charged and H-charged specimens in step-wise creep and normal tensile tests are shown in Fig. 3(a). The effects of solute H clearly appeared as constant increases in yield and flow stress with an extent of almost 50 MPa. Taken as 0.2 % proof stress, $\sigma_{0.2}$, the yield stress was 250 MPa for the non-charged specimen, while it was 300 MPa for the H-charged specimen. The horizontal parts on the stress-strain curves correspond to the 1000 s load-holding and resultant strain by creep deformation, ε_c. Importantly, the stress-strain curves in normal tensile and stepwise creep tests coincided well with each other except for the crept parts, indicating that the intermediate creep deformation does not significantly affect the overall stress-strain behavior. The true stress-strain curves were derived from the monotonic deformation curves in Fig. 3 (a) and their work-hardening characteristics are analyzed in Fig. 3(b). The details of Fig. 3(b) will later be explained in Section 4.1.

Fig. 4 shows the creep strain versus time curves of (a)(c) non-charged and (b)(d) H-charged specimens at various stress and strain. Both the non-charged and H-charged specimens started to exhibit minute creep deformation when the stress reached slightly below their yield stresses, *i.e.*, 200 MPa for non-charged and 250 MPa for H-charged specimens,

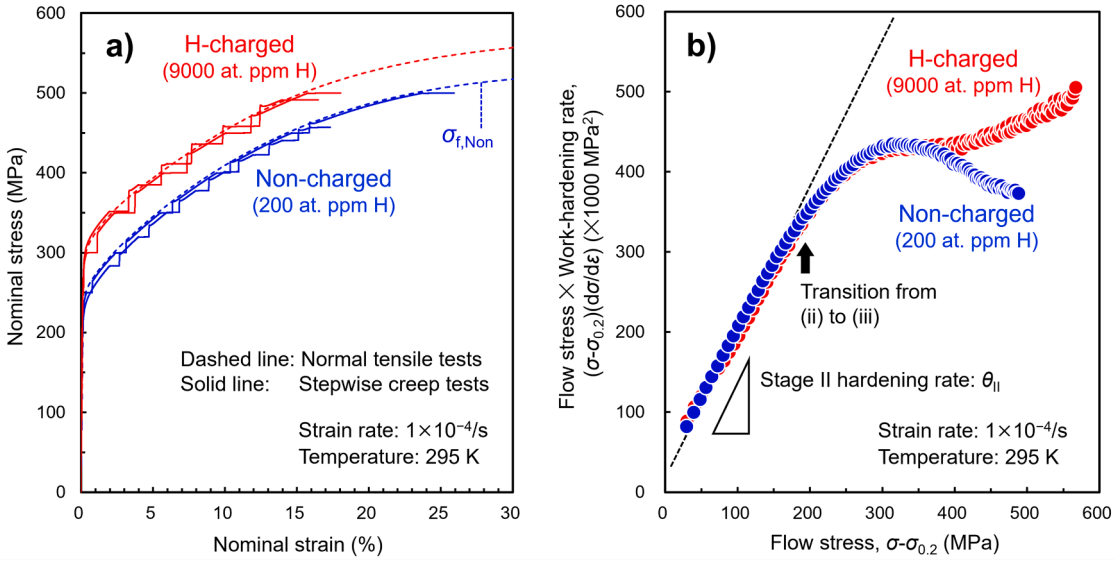

Fig. 3. (a) Nominal stress-strain curves of non-charged and H-charged Type310S steel during normal tensile and stepwise creep tests at 295 K. The horizontal parts on the solid lines correspond to the creep strain during 1000 s load-holding. (b) work-hardening characteristics during monotonic tensile tests analyzed by the method proposed by Mecking and Kocks [82,83] (see Section 4.1 for the interpretation of this diagram).

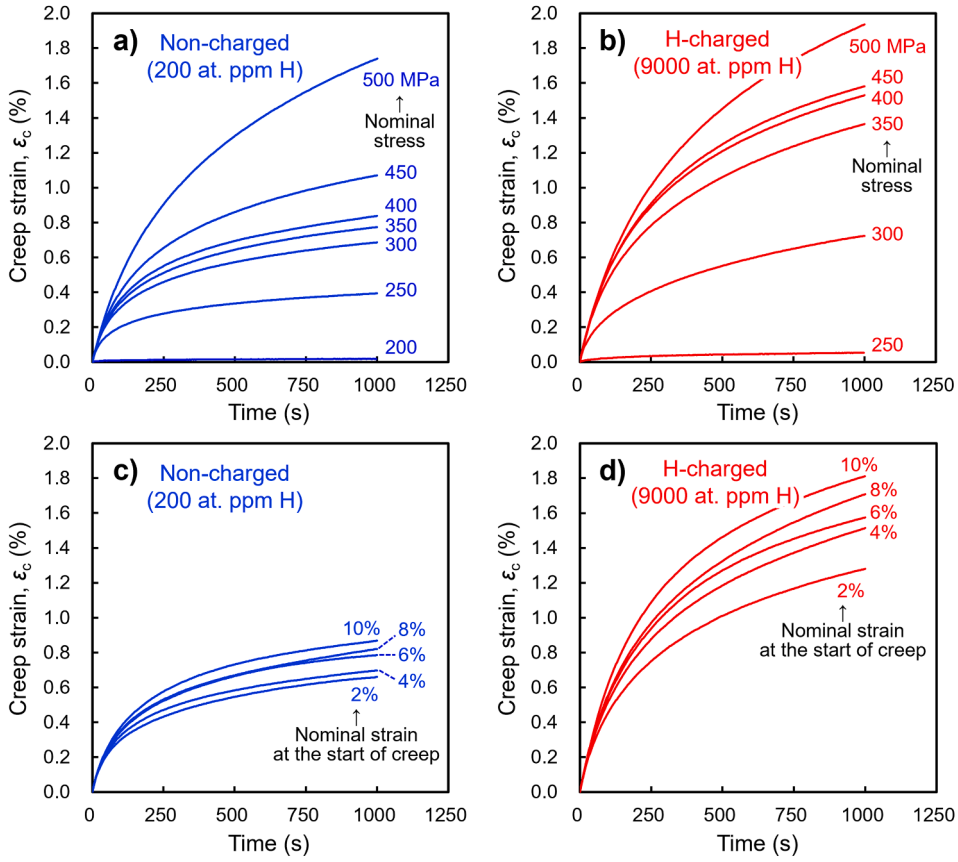

Fig. 4. Creep curves of (a)(c) non-charged and (b)(d) H-charged specimens in stepwise creep tests (cf. Fig. 2(a) and Fig. 3(a)). The behavior of non-charged and H-charged specimens can be compared under some fixed (a)(b) nominal stresses and (c)(d) strains.

respectively. With the increases in applied stress and strain, the amount of creep deformation within 1000 s monotonically increased. In the low-stress regime around the yield point (*e.g.*, 250 MPa in Fig. 4(a) and (b)), the creep strain in the H-charged specimen was rather smaller than that in the non-charged specimen. However, the trend was reversed as the applied stress and strain escalated, rendering the creep deformation in the H-charged specimen larger than that in the non-charged specimen. Such an H-effect was profound at the stress of 350~450 MPa and the strain of 2~10 % (Fig. 4). These changes in the flow behavior during normal tensile and creep tests were not observed in specimens merely

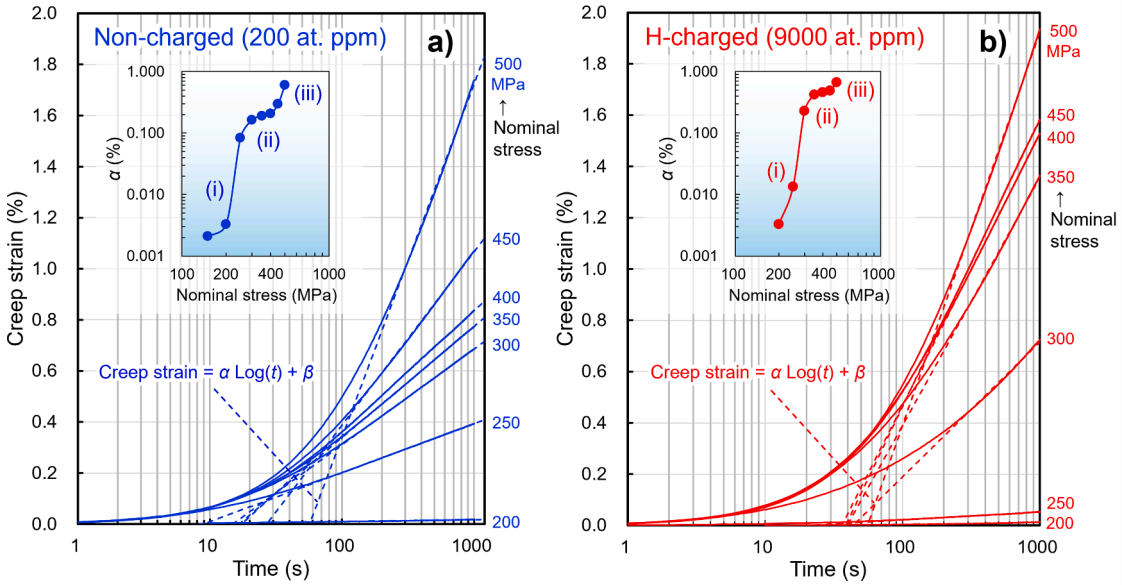

Fig. 5. Creep strain versus log-time curves in (a) non-charged and (b) H-charged specimens corresponding to the results shown in Fig. 4(a) and (b). The creep curves obeyed logarithmic time law after the initial transition period of about 100 s, the time coefficient of which is plotted as a function of applied nominal stress in the insets.

heat treated in air at 543 K. This demonstrates that the present characteristics in H-charged specimens stem from an intrinsic impact of solute H rather than any structural changes due to exposure to high temperature (Appendix A1). The enhancement of the magnitude and rate of creep under a fixed stress or strain condition is reminiscent of similar H-impact on the same steel type in the past experiments [30,66].

The data in Fig. 4(a) and (b) were converted into creep strain versus log-time curves and reproduced in Fig. 5. After the initial transition period of 100~200 s, all the creep curves obeyed a logarithmic time law (*i.e.*, $\varepsilon_c = \alpha \mathrm{Log}(t) + \beta$, where α and β are constants), which is a typical behavior of transient creep [84,85]. The time coefficient α, a parameter characterizing the creep rate, was determined from the straight part of each creep curve and plotted against the applied nominal stress in the insets of Fig. 5. (i) Sharp increase of α was identified around the yield point, whereas (ii) its escalation became much slower at an intermediate stress. (iii) When the stress becomes further greater, α tended to show a sharp increase again. α in the H-charged specimen was higher than that in the non-charged specimen particularly in the regime (ii), reflecting an accelerated creep deformation under the presence of H.

3.2. Creep deformation after pre-straining and stress-dip

The load versus nominal strain curves during the pre-straining to 10 % (*i.e.*, strain regime where H-effect on the creep was most substantial) are depicted in Fig. 6(a). After this pre-straining, stepwise reloading with a 1000 s load-holding for each was implemented, as the load-time curves are shown in Fig. 6(b). The applied true stresses were within the range of 200~420 MPa for the non-charged specimen and 200~460 MPa for the H-charged specimen. Some representative creep strain-time curves at several stress levels are presented in Fig. 6(c) and (d).

The non-charged specimen started to creep at 300~350 MPa (Fig. 6 (c)), a stress level well below the maximum stress during the pre-straining (Fig. 6(b)). The creep strain monotonically increased with an escalation of applied stress. On the other hand, the H-charged specimen also started creeping at an equivalent stress level to the non-charged specimen (Fig. 6(d)). The magnitude of creep strain at such low stresses was extremely low (<0.01 %), where differences between H-charged and non-charged specimens were unclear. However, what should be emphasized in Fig. 6 is the creep behavior at the stress levels of 400~440 MPa. That is, while the creep deformation gradually became substantial in the non-charged specimen, that in the H-charged specimen remained smaller until the stress reached 440 MPa. Only when the applied stress well exceeded the flow stress in the non-charged specimen during its pre-straining, $\sigma_{f,non}$, significant creep deformation, the magnitude of which was greater than that in the non-charged specimen, was observed in the H-charged specimen (*e.g.*, at 460 MPa).

Such an inhibitory effect of H on the creep deformation was also evidenced by the result of an additional test involving rapid stress-dip (Fig. 7). After the stress-reduction toward the almost equivalent level with $\sigma_{f,non}$, the H-charged specimen exhibited considerably small creep strain with the order equivalent to those at 350~440 MPa in Fig. 6(d), despite significant creep in the non-charged specimen at an identical stress-strain conditions. Notably, our systematic experimental framework so far successfully discovered stress-dependent antagonistic H-effects on the magnitude and rate of creep deformation at room temperature, which has not yet been uncovered in previous studies.

3.3. Flow stress components

The true stress-time curves in successive stress-dip tests are presented in Fig. 8. As examples, a part of each curve is magnified and shown in the insets, demonstrating that the relaxation direction changed from forward to backward at a certain point. These turning points of relaxation direction, σ_i, where some dislocations start backward motion, (or the points at which relaxation became zero) were extracted and plotted against true strain in Fig. 9. The gap of internal stress, σ_i, in non-charged and H-charged specimens was quite small as compared with the difference in their flow stress. Moreover, internal stress in the H-charged specimen is always laid below the flow stress in non-charged specimen. This fact means that a major part of the flow stress gap between non-charged and H-charged specimens stems from the contribution of solute H on the effective stress, σ_{eff}.

3.4. Evolution of internal structures

The ECCI micrographs of the dislocation structures in non-charged and H-charged specimens deformed to 10 % nominal strain are presented in Fig. 10(a) and (b). These two imaged grains have mutually

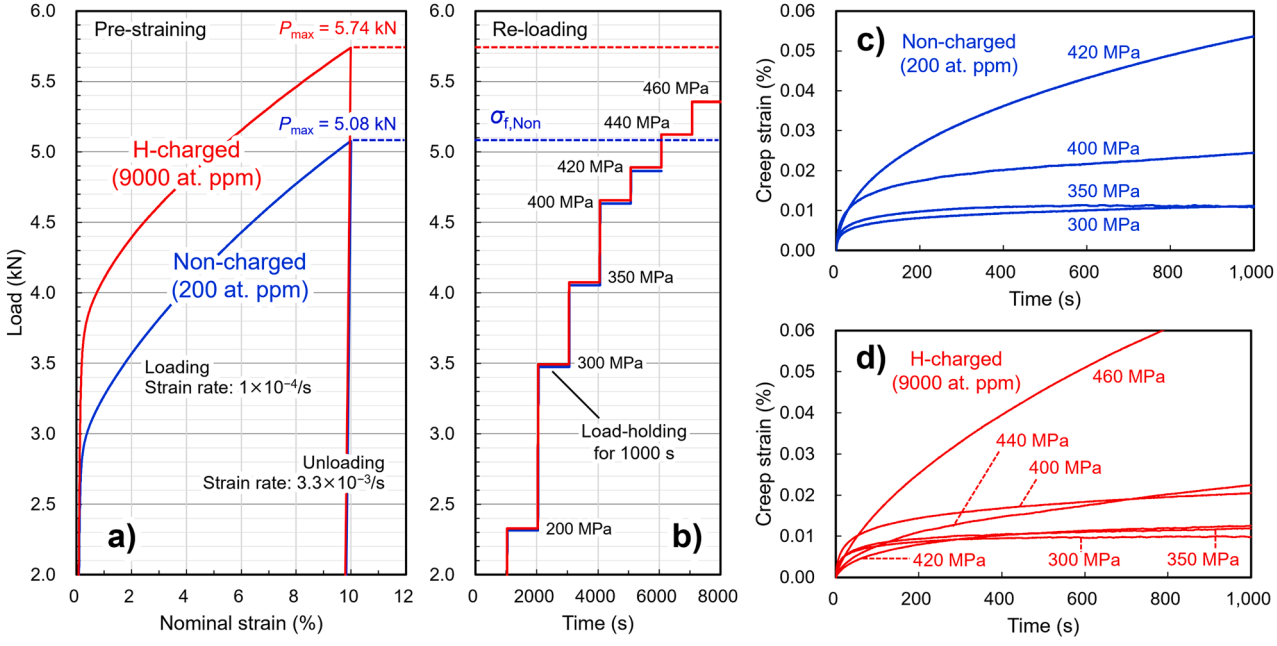

Fig. 6. Creep tests after pre-straining to 10 % nominal strain. (a) and (b) are the applied load-nominal strain curves during pre-straining and load-time curves during re-loading, respectively. The creep curves in the load-holding phases during re-loading are depicted in (c) and (d) for non-charged and H-charged specimens.

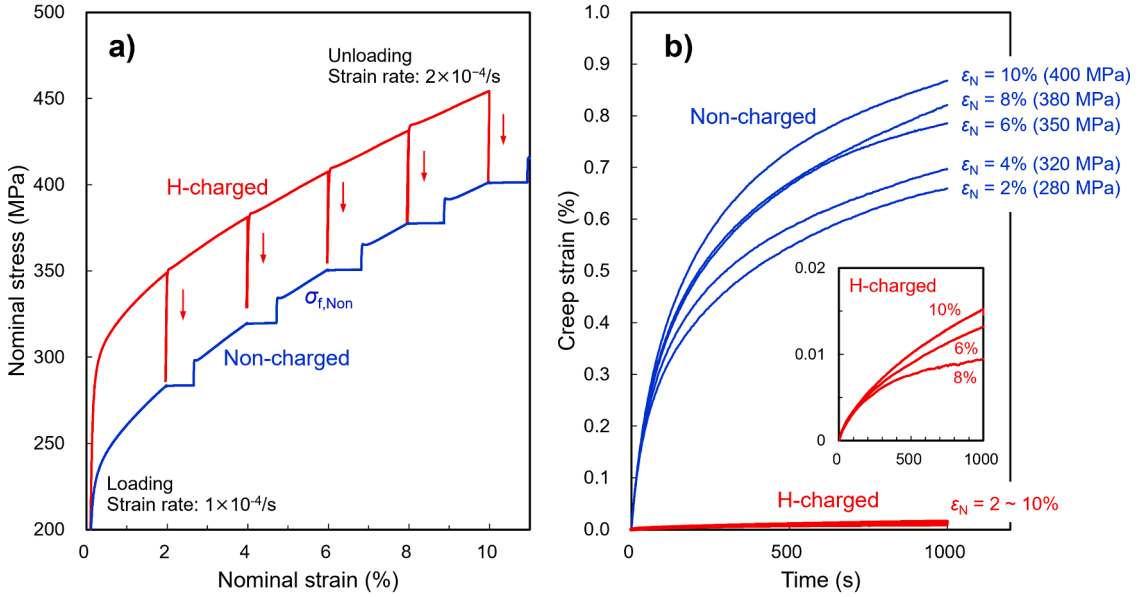

Fig. 7. Creep test of the H-charged specimen, which involves partial unloading to the stress level identical to that in the non-charged specimen. After each unloading process, the load was held for 1000 s. (a) shows the nominal stress-strain curves in the test, while creep curves during the load-holding are depicted in (b).

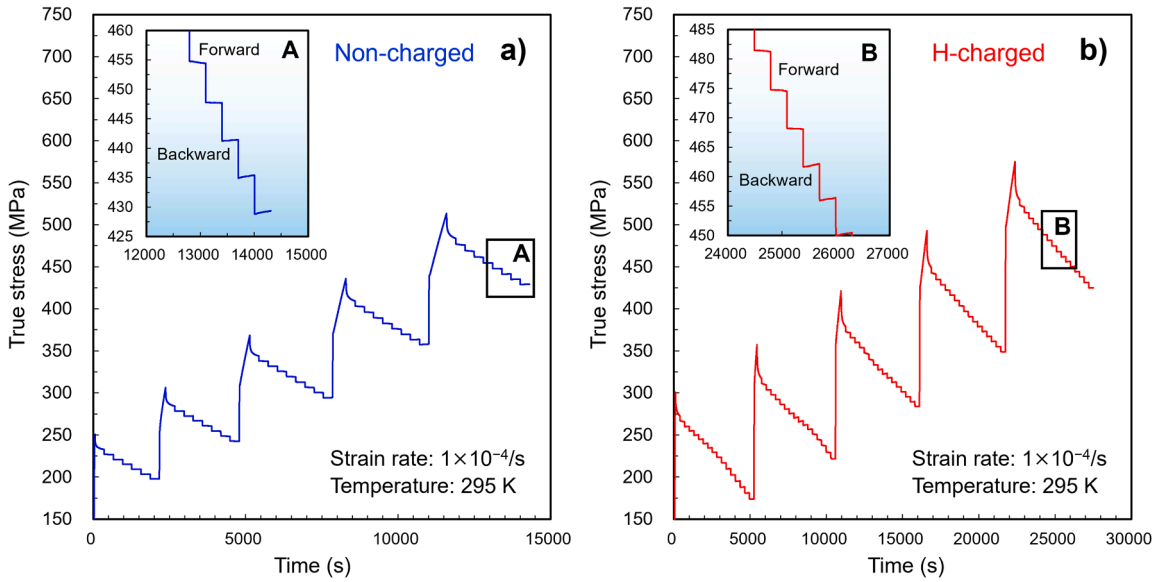

Fig. 8. True stress versus time curves of (a) non-charged and (b) H-charged specimens in the successive stress-dip tests. The insets magnify the parts surrounded by the rectangles A and B, showing the change of stress relaxation direction from forward to backward.

similar tensile axes close to <111>-pole in a stereographic triangle, and 111 diffraction vectors were used for their imaging under two-beam conditions. The orientations of diffraction vectors and the traces of {111} crystal planes are also included in the micrographs.

No profound differences in the arrangement of dislocations were found between non-charged and H-charged specimens. In both cases, dislocations were heavily tangled to such a degree that individual dislocation lines were hard to be discerned. They exhibited organized structures involving dense dislocation walls as well as dislocation cells, where walls and cell boundaries were primarily aligned parallel to {111} slip planes. These types of dislocation arrangements were consistently observed in many parts of the deformed samples.

The absence of any substantial H-effect on the dislocation structure evolution under a given strain is more statistically evidenced in the Vickers hardness measurement. As shown in Fig. 10(c), the samples with 10 % nominal strain exhibited an identical hardness within the range of error bands regardless of the presence and absence of solute H (for the H-charged specimen, all the solute H was desorbed by heating at 500 K after deformation (Section 2.4)). Note that the hardness of non-charged specimens with 10 % strain remained constant before and after annealing at 500 K, while it clearly increased compared with the non-deformed sample. This indicates that the heating at 500 K did not cause any significant changes and recovery of the deformation microstructure.

4. Discussion

The room temperature creep in Type310S steel consistently obeyed a logarithmic time law, *i.e.*, $\varepsilon_c, = \alpha \mathrm{Log}(t) + \beta$, which is a typical behavior of transient creep (Fig. 5). With the increases in applied stress and strain,

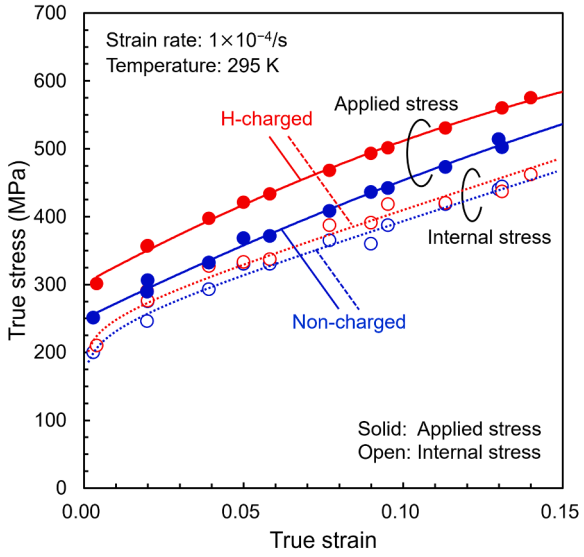

Fig. 9. Applied stress and internal stress in non-charged and H-charged specimens plotted against true strain. The data were measured by successive stress-dip tests (Fig. 8).

the coefficient α exhibited a monotonic increase accompanying three distinctive stages (*i.e.*, stages (i)~(iii) in Fig. 5) in both non-charged and H-charged specimens. In this section, the origins of these three stages are first described apart from the H-effects. Then, the discussion will move on to the influence of solute H.

4.1. Stages of room temperature creep

The decay of creep rate similar to the initial transition of α (Stages (i)~(ii) in Fig. 5) has been observed in the room temperature creep of Type304 and other austenitic stainless steels [64,70,86]. Thus, the behavior should not be unique to the present Type310S but rather universal in various austenitic steels with similar Fe-Cr-Ni-based compositions.

Tendo et al. reported that the shallow slope of the α-stress plot in stage (ii) starts to appear at the stress level close to 0.2 % proof stress [70]. From this fact, they ascribed the stage (i)-to-(ii) transition to the effect of work-hardening. Namely, a prompt increase in dislocation density after yielding increases the frequency of dislocation-dislocation interactions, shortening the mean free path of individual dislocations during the creep. This effect compensates for the influences of increasing stress (*i.e.*, driving force for creep deformation) and increasing mobile dislocation density (*i.e.*, carriers of plasticity) in stage (ii), although these two factors effectively work to enhance the creep rate in stage (i). According to the characterization by Feaugas on Type316L steel [78], dislocations readily exhibit planar pile-up and multi-slip accompanying dislocation junctions between intersecting slip systems at a strain of around 1 %. Above this small strain, those dislocations rapidly evolve into wall and cell structures like Fig. 10. The long-range repulsive force between pile-up dislocations, as well as some extra work required for cutting the intersecting forest dislocations [73–75], could retard the movement of mobile dislocations in stage (ii).

The α regained its sharp increase in stage (iii) (Fig. 5). This third stage might be due to a phenomenon specific to a large plastic strain regime such as dynamic recovery [71,82]. Mecking and Kocks enabled the identification of the onset of dynamic recovery in polycrystalline FCC metals and alloys analogous to the Stage II and Stage III hardening in single crystals [82,83]. Their method is to simply plot the product between true stress, σ, and work-hardening rate, $d\sigma/d\varepsilon$, against true stress, assuming that the stress-strain behavior of the material obeys the conventional Voce law.

$$\sigma\frac{d\sigma}{d\varepsilon} = \sigma(\theta_{II} - \theta_r) \tag{1.a}$$

Here, θ_{II} is the athermal hardening rate corresponding to the Stage II linear hardening in FCC single crystals, and θ_r is the dynamic recovery term that decays the work-hardening rate. In the initial stage of deformation, the slope of $\sigma(d\sigma/d\varepsilon)$-$\sigma$ plot is solely controlled by θ_{II}. On the other hand, the slope gradually decreases with an increasing contribution of θ_r. When there exist significant stress contributions from grain boundaries and solutes that are assumed to be independent of strain (*i.e.*, they only contribute to the yield stress, $\sigma_{0.2}$, as an approximation), eq. (1.a) can be modified as:

$$(\sigma - \sigma_{0.2})\frac{d\sigma}{d\varepsilon} = (\sigma - \sigma_{0.2})(\theta_{II} - \theta_r) \tag{1.b}$$

Fig. 3(b) shows such $(\sigma-\sigma_{0.2})(d\sigma/d\varepsilon)$-$(\sigma-\sigma_{0.2})$ plots of non-charged and H-charged specimens during the normal tensile tests shown in Fig. 3(a). After the onset of plastic deformation, the $(\sigma-\sigma_{0.2})(d\sigma/d\varepsilon)$ linearly increased with a slope, θ_{II}. Eventually, the $(\sigma-\sigma_{0.2})(d\sigma/d\varepsilon)$-$(\sigma-\sigma_{0.2})$ curves deviated from the linearity and showed concave downward owing to an increase of dynamic recovery term, θ_r. The black arrow in Fig. 3(b) indicates the $(\sigma-\sigma_{0.2})$ value approximately corresponding to the nominal stresses in the insets of Fig. 5, at which the transition from stage (ii) to (iii) commenced. The arrow is well coincident with the points where $(\sigma-\sigma_{0.2})(d\sigma/d\varepsilon)$-$(\sigma-\sigma_{0.2})$ curves deviate from θ_{II} slope. This coincidence proves that the increase in creep rate in

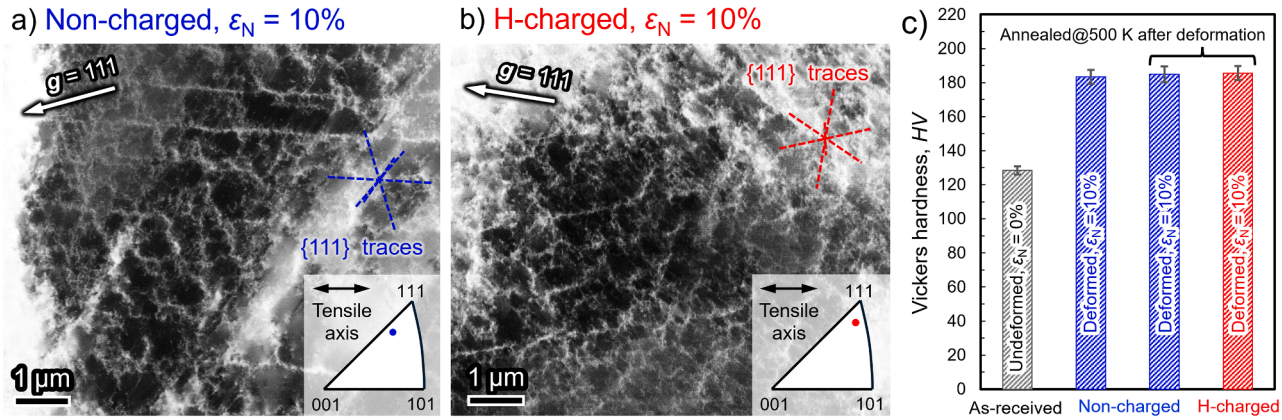

Fig. 10. (a)(b) ECCI micrographs of the dislocation structures in (a) non-charged and (b) H-charged specimens deformed to 10 % nominal strain. The tensile axes of the imaged grains are shown in the insets. ***g*** denotes the diffraction vectors used for imaging. The Vickers hardness of those samples, as well as of as-received material, are plotted in (c). The error bars in (c) indicate the standard deviation in 20-point measurements.

stage (iii) stems from dynamic recovery, counterbalancing the effect of work-hardening to retard the creep.

4.2. Apparent and intrinsic effects of solute H on plastic flow

The creep behavior changed drastically when H was involved (Sections 3.1 and 3.2). On the other hand, the development of deformation microstructure was not significantly affected by H, although such confirmation was only made at a strain of 10 % (Fig. 10). The invariance of dislocation arrangement reproduces the author's past results where influences of H on the substructural development in Type310S steel was examined more precisely [59,69,87,88]. Our TEM observations and careful examinations of work-hardening behavior revealed that the influence of H on dislocation structure evolution and arrangement is minor. Moreover, the three creep stages (i)~(iii) were common in both non-charged and H-charged specimens (Fig. 5). These facts indicate again that the influences of solute H on creep stem primarily from the increase/decrease in the mobility of individual dislocations rather than any changes in their collective behavior. The invariance of internal stresses shown in Fig. 9 also supports the absence of an H-effect on the dislocation arrangement. Potentially, presently found H-impacts on creep behavior would monotonically be amplified with an increase in H concentration up to 10,000 at ppm, although only one concentration was examined here. Such an expectation can be made from an almost linear H concentration-dependence of the magnitude of solid solution-hardening by H in this concentration range [35,36].

Beyond the relevant past studies highlighting only the enhancement of creep in the H-charged austenitic steels [30,66], Fig. 4 to Fig. 7 enable us to draw the following statements to phenomenologically describe the two opposite, stress-dependent influences of solute H manifesting beyond the yield stress.

(1) *Creep is accelerated in the presence of H* at either fixed stress or fixed strain.
(2) *Creep is retarded in the presence of H* when both the strain and stress are fixed.

The fact (1) implies an apparent H-effect accelerating the creep. However, here we have to remember the description given in Section 4.1: *the rate and magnitude of creep depend on the synergistic contributions of applied stress (driving force for creep deformation), mobile dislocation density (carrier of plasticity), and work-hardening (obstacles against deformation)*. In this context, the essential role of solute H seems more straightforward in the statement (2). That is, while (1) H apparently enhances creep when load-holding is implemented during monotonic deformation, (2) H can retard creep by decreasing the mobility of individual dislocations. The key and novel experimental finding in the present research is that the superficial H-effect (1) appears only when a certain stress criterion is satisfied, as discussed in the following sections.

4.3. Rate-controlling processes of creep

At first glance, the retardation of creep by H aligns with our stress relaxation experiments [59]. In reference [59], we have intimated that H atoms segregated along a dislocation line act as short-range obstacles, which are more sensitive to thermal activation than other obstacles

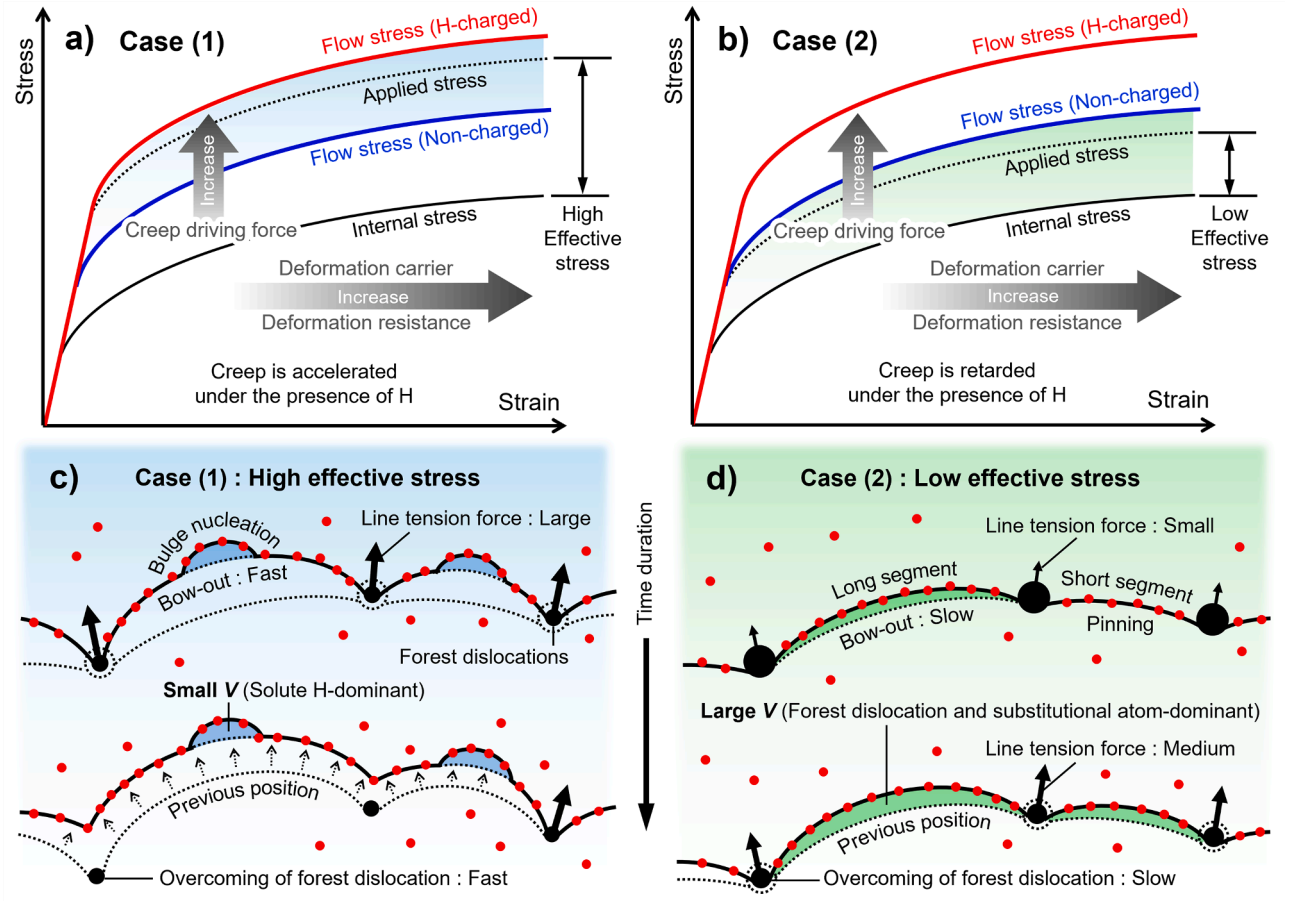

Fig. 11. Summary of the H-effects on plastic flow: (a)(b) stress-strain curves showing the two distinct regimes for creep under (a) high and (b) low stresses. (c) and (d) show the different rate-controlling processes of thermally activated dislocation motion when the applied stress lay within the blue and green regimes in (a) and (b), respectively.

originally involved in the material. As such, it is the effective stress required to overcome these newly involved obstacles, H, that causes the constant increase in the flow stress (*i.e.*, solid solution-hardening) during the tensile test (Fig. 3(a)). Meanwhile, in relation to such solid solution-hardening, the superficial H-effect to accelerate the creep manifested only when the applied stress well exceeded the flow stress in the non-charged specimen, $\sigma_{f,non}$: blue-shaded area in the illustration in Fig. 11(a), where effective stress stemming from solute H is overridden on the flow stress of non-charged specimen. We now attempt to rationalize these seemingly contradicting roles of H on creep deformation in terms of the stress-dependent change of rate-controlling obstacles.

4.3.1. Obstacle types responsible for creep rate

A physical parameter frequently used to characterize short-range obstacles is their activation volume, V_a [2,3,7,13]: a product between Burgers vector, b, and the area swept by dislocation during its thermal activation event. Given that the plastic deformation obeys the Arrhenius-type rate equation [1,2], the V_a of the rate-controlling obstacles for creep can be determined as follows [7].

$$\Delta\gamma_c = \left(\frac{kT}{\theta V_a}\right)\ln\left(1+\frac{t}{C_c}\right) \tag{2}$$

where $\Delta\gamma_c$ is the shear strain (*i.e.*, tensile strain multiplied by Taylor factor of 3.06), k is Boltzmann constant, T is temperature, θ is work-hardening rate (also converted into shear form by assuming Taylor factor), t is creep time, and C_c is constant. By fitting the creep curves in Fig. 4 with adjustable parameters V_a and C_c, V_a was calculated in Fig. 12 (a). The appropriate value of θ for eq. (2) can be determined from the work-hardening rate immediately before the start of creep or from the monotonic tensile deformation curve at a similar strain. However, the same procedure is inapplicable to low stress/strain, where plasticity is highly inhomogeneous [89] and the slope of the stress-strain curve is close to the elastic modulus. Thus, at the stresses below and close to $\sigma_{0.2}$, θ was approximated by Stage II hardening rate ($\theta_{II} \approx 1800$ MPa in Fig. 3 (b)), assuming that multi-slip takes place from the beginning of plasticity in polycrystalline material.

Large V_a of $>1000b^3$, similar orders in pure FCC metals and dilute alloys at low stresses [13,14,90,91], was measured at a low strain around the yield point, possibly reflecting the interaction of mobile dislocations with forest dislocations [3]. V_a rapidly decreased to several hundred b^3 with an increase in strain to 0.01. This sharp initial decrease might be due to the prompt multiplication of dislocations [89,92] and a decrease in their link length. Then, the strain-dependent decrease in V_a became minute as the strain level went into the stage (ii) creep regime where superficial H-effect was most prominently observed (Fig. 4 and Fig. 5). In stage (ii), V_a in both non-charged and H-charged specimens were insensitive to strain. The latter was consistently smaller than the former, resembling the H-induced reduction of V_a in stress relaxation experiments [59,60]. These smaller and strain-independent V_a imply that denser obstacles, which have strain-independent concentration and a character more sensitive to thermal activation, are the main rate-controlling factors for the creep in the H-charged specimen. Duplicating our previous statement [36,59,60], such denser obstacles here are certainly solute H themselves. Instead, V_a of $\approx 200b^3$, which is larger than the H-charged case but still relatively small, implies that the major rate-controlling obstacles may be substitutional solutes in the non-charged case. They may become more predominant than forest dislocations when the applied stress is high.

On the contrary, an opposite effect of H on V_a was newly found in pre-strained specimens (Fig. 6) in association with the creep retardation. Under the stress level below $\sigma_{f,non}$, solute H somewhat increased V_a (Fig. 12(b)). The dimension of V_a was also much larger than those at the same strain level in Fig. 12(a), lying in the same order with the stage (i) creep. V_a sharply decreased as the applied stress exceeded $\sigma_{f,non}$. Eventually, V_a in the H-charged specimen fell below the non-charged specimen as for the case of references [59,60].

4.3.2. Model of dislocation motion

Summarizing the preceding discussions, the requirement for the superficial H-effect to accelerate the creep can be concluded as follows: *under a given strain, the applied stress must significantly be higher than the flow stress in the absence of H:* $\sigma_{f,non}$ (*i.e.*, blue-shaded area in Fig. 11(a)). Under such a circumstance, the main rate-controlling process for dislocation motion is to overcome H atoms themselves that accompany a smaller activation volume. The authors have preliminarily proposed an interaction model between solute H and mobile dislocations [59] based on the *trough model* of solid solution-hardening established by Kocks [14]. Admirably, both the H-effects to accelerate and retard creep deformation depending on the stress provides some additional, powerful

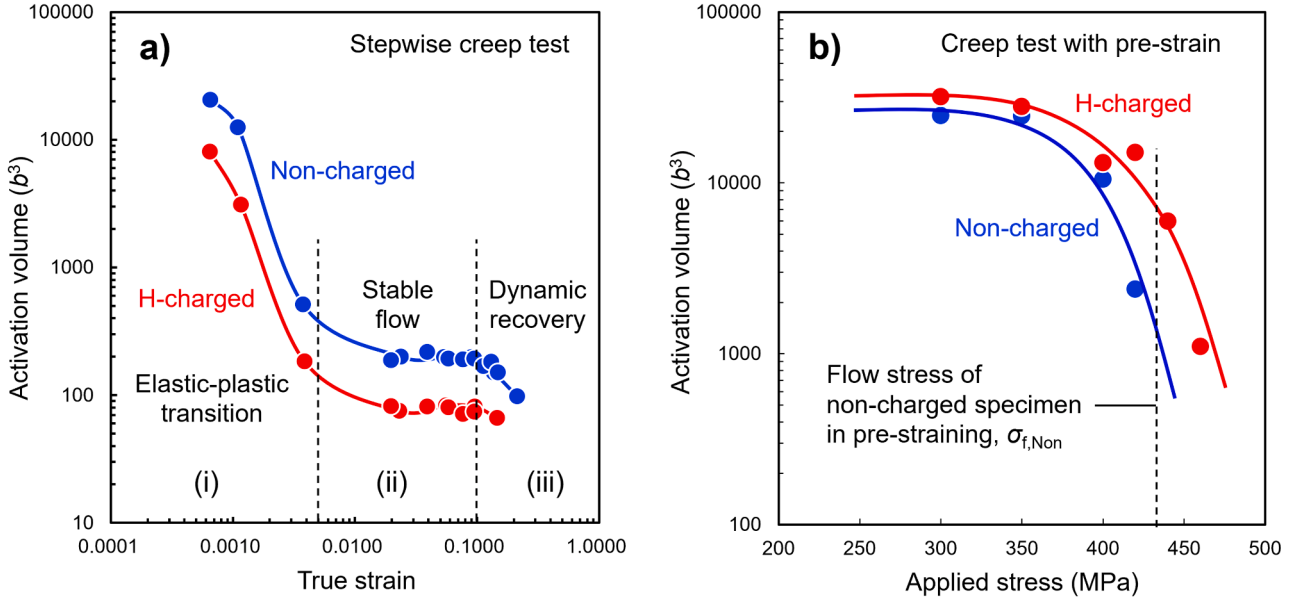

Fig. 12. Activation volume, V_a, of the rate-controlling obstacles in (a) stepwise creep tests and (b) creep tests after pre-straining. Calculation of V_a was done by fitting the creep curves in Fig. 4 and Fig. 6(c)(d) with eq. (2).

verifications for our model.

A schematic of the H-dislocation interaction model is reproduced in Fig. 11(c). During the bow-out of a dislocation segment between forest dislocations, diffusible H atoms dynamically segregate close to the dislocation core and obstruct the dislocation movement. Such a dynamic segregation of H was theoretically confirmed under a similar H concentration, temperature, and strain rate (*i.e.*, below 10^{-4}/s during the creep) condition [36,59]. These segregated H reduce the line energy of dislocation [93], rendering the dislocation as if it lays along a bottom of energy trough [14]. With the aid of applied stress and thermal vibration, the dislocation moves forward *via* creating a small bulge, an activation volume of which is small. The size of these bulges is a direct function of local H concentration along the dislocation core and a resultant magnitude of line energy reduction [14,59]: the higher the H concentration, the smaller the bulge size and activation volume, as was confirmed experimentally [59,60]. Possibly, an obstruction to the bulge nucleation process stems from an energy barrier against the stress-assisted diffusion jump of H from the dislocation core to the direction of dislocation motion. This diffusion-controlled glide process is analogous to the micro-creep model proposed by Friedel [94]. Note that the bowing-out also requires successive overcoming of substitutional solutes as background friction, although it is omitted in Fig. 11(c) for simplicity.

Indirect but plausible evidence to support the applicability of trough model is the phenomenon called *stress-equivalence* [13] figured out in the authors' previous stress relaxation study [59]. That is, the yield stress, σ_y, was a unique function of V_a irrespective of the presence and absence of solute H in analogous to the original report by Basinski et al. [13] who identified a unified law of $\sigma_y \sim (1/V_a)^m$ (m is a constant) in copper alloys containing various solute species and concentrations. Amongst a number of models of solute-dislocation interactions, only trough model can reasonably rationalize such a sole dependence on V_a since it assumes dislocation line energy, which is reduced by solutes, as an exclusive parameter determining σ_y [14]. Considering the high mobility of solute H that enables its coordinative motion with dislocation, we incorporated diffusion energy barrier of H to migrate with the dislocation segment bulging from the solute row. The validity of this idea has to be tackled further in our forthcoming studies. For instance, measurement of the creep activation energy and its comparison with the energy for bulk H diffusion potentially provides us how significant the diffusion jump of H contributes in progressing the deformation. Another important implication in stress-equivalence and trough model is that the elemental activation process should involves plural solute atoms, which is also inferred in the H-charged austenitic steel having the V_a of the order of $100b^3$ (*e.g.*, Fig. 12(a) and [59,60]).

Note that the present H-dislocation interaction model in Fig. 11(c), (d) is applicable only to the deformation at the temperatures close to an ambient condition. If the temperature becomes higher so as the thermal activation process to move the dislocation is further aided by amplified atomic vibration, as well as local H concentration along dislocation line (*i.e.*, obstacle density) is also diluted, influence of H on creep will eventually disappear. This can be evidenced in our past study on the tensile properties of an H-charged Type310S steel, where H-induced solid solution-hardening indeed lost above 400 K [36]. On the other hand, at the temperatures well below 295 K, the model in totally breaks down because the coordinative movement of H with dislocations becomes infeasible. Under such a circumstance, movement of dislocations is controlled by their statistical encountering and interaction with H atoms randomly dispersed throughout the lattice, the creep behavior in which needs to be investigated further.

4.3.3. Roles of obstacle solute H

4.3.3.1. Case (1): faster creep rate under high stress. In order to understand the deformation kinetics of a material under its work-hardened state, one must consider simultaneous interactions of a mobile dislocation with solute atoms and forest dislocations [95,96], the latter of which is newly involved in our model as depicted in Fig. 11(c)(d). Due to the small activation volume, the overcoming of segregated H progresses rather fast (*i.e.*, fast creep rate) because thermal activation acts more effectively in aiding it [10,96,97]. This causes a relatively large bow-out and curvature of the whole dislocation segment between the trees, giving rise to considerable local forces acting on the trees due to dislocation line tension (upper half of Fig. 11(c)) [96]. Accordingly, the dislocation can readily penetrate the trees (lower half of Fig. 11(c)), as well as substitutional solutes. The waiting time for overcoming those intrinsic obstacles *via* thermal activation is no longer significant once the applied stress well exceeds $\sigma_{f,non}$ such that the effective stress becomes critical for these sequential processes. In a similar manner, substitutional solutes are more rate-controlling than forest dislocations in the non-charged case when stress is high enough, leading to the strain- (*i.e.*, dislocation density-) insensitivity of the activation volume (Fig. 12(a)). It seems that the assumed local stress acting on the trees conflicts with the lowered line energy by segregated H. However, those H atoms distribute very close to the dislocation core (radius of 2∼3b) at room temperature [36], maintaining the line energy stemming from the long-range stress field around the dislocation unchanged.

In the context of the model in Fig. 11(c), one can argue that *the H-effect in terms of the flow stress is to put an additional thermal stress onto the original intrinsic flow stress of the material* (Fig. 11(a)). The former is the stress required for bulging from an array of H, whereas the latter is for bowing-out between the forest dislocations as well as for overcoming substitutional solutes. The equivalence of internal stresses between non-charged and H-charged specimens shown in Fig. 9 reasonably conforms to this idea. Additionally, the primary dependence of the bulge size on H concentration can rationalize the strain-independent activation volume in stage (ii) creep (Fig. 12(a)) and a parallel upward shift of the entire stress-strain curve in the H-charged specimen (Fig. 3(a)).

4.3.3.2. Case (2): retardation of creep under low stress. The effective stress acting on the dislocation may not be enough to make the bulge nucleation a frequent event when the applied stress is below or close to $\sigma_{f,non}$ (Fig. 11(b)). As such, segregated H does nothing other than obstruct the dislocation movement in cooperation with other intrinsic obstacles. The dislocation segment loses its mobility, although it was originally able to bow-out faster in the absence of H. Due to such immobilization, plasticity must be carried by other dislocation segments, that have longer link length and ease of bow-out even under such H-induced obstruction effect and lower stress level (Fig. 11(d)). Since the bow-out displacement could also become smaller owing to the lower stress, the local force acting on the trees also becomes smaller. Thus, the overcoming of forest dislocations, which accompanies a larger activation volume, takes a longer time and becomes a primary rate-controlling process for creep (Fig. 11(d)). This is the situation precisely the cases in Fig. 6 and Fig. 7, where the creep rate was retarded under the presence of H. Similarly, the rate-controlling process in the non-charged specimen also changes to overcoming forest dislocations at low stress, resulting in an activation volume greater than $1000b^3$ (Fig. 12(b)). In other words, the magnitude of bow-out acts as a critical parameter determining the probability of overcoming their forest anchoring points in this model. Thus, non-charged and H-charged specimens may exhibit mutually identical creep rate if the dislocation segments with a given link length, which are contained in these two samples, can bow-out in the same magnitude. Such a situation should be satisfied when applied stress in H-charged specimen is somewhat larger than that in non-charged one owing to the inhibitory effect of H on dislocation motion.

Although the present description still remains qualitative, it can well account for the seemingly contradicting H-effects on room temperature creep. The model in Fig. 11(c) has also been validated based on the H concentration- and stress/strain-dependencies of V_a during our stress

relaxation tests [59]. Some additional investigations, such as stress-dependence of activation volume or evaluation of temperature effects, can provide more pieces of information to comprehend the complex H-dislocation interactions. Finally, one has to emphasize that our result does not contradict the report by Tien and Altstetter, who performed pioneering work on the creep of H-charged Type310S steel [30] (Section 1). The smaller creep strain at the beginning and the longer creep duration can also be viewed as a delay of creep by newly involved short-range obstacles: H.

5. Conclusions

The plastic flow behavior of a Fe-24Cr-19Ni-based Type310S austenitic steel uniformly charged with 9000 at ppm H was studied *via* room temperature creep experiments at 295 K. With the information of work-hardening behavior, dislocation structures, flow stress components (*i.e.*, effective and internal stresses), and activation volume reflecting the rate-controlling obstacle types, the following influence of solute H on thermally activated deformation and its stress-dependence were identified.

1. Solute H works as a short-range, thermally activatable obstacle to dislocation motion without impacting on the development of collective dislocation structures, causing a solid solution-hardening with an extent of 50 MPa. Such a magnitude of strengthening primarily stems from the contribution of H to the effective (thermal) stress component. This understanding of the role of H agrees with our previous results based on stress relaxation experiments of the same material.
2. Dual H-effects on creep rate and size of activation volume were observed depending on the level of applied stress. When the applied stress is well exceeding the flow stress in the absence of H, $\sigma_{f,non}$, the creep rate in the H-charged material was accelerated with respect to that under non-charged condition, and the activation volume accordingly decreased: Case (1). Meanwhile, once the applied stress falls close to or below $\sigma_{f,non}$, the H-effect turns into a retardation of creep rate and an enlargement of activation volume: Case (2).
3. Taking solute H as a short-range obstacle, the above two opposite H-effects on creep behavior can be interpreted as follows.

   Case (1): Effective stress, a driving force of thermally activated deformation, is sufficiently large so that the material's intrinsic short-range obstacles (*i.e.,* forest dislocations and substitutional solutes) are readily penetrable by dislocations. As such, the predominant rate-controlling process for dislocation motion is to overcome newly involved obstacle type: solute H with the aid of thermal activation. Due to a smaller activation volume involved in this process of overcoming H, resultant creep rate becomes faster.

   Case (2): Effective stress is insufficient for thermally activated overcome of solute H to be a frequent event. Thus, H hinders dislocation motion in cooperation with other intrinsic obstacles. Owing to this retardation effect, the mobile dislocation segment under a given applied stress potentially becomes longer, increasing the activation volume and decreasing the creep rate.

CRediT authorship contribution statement

Yuhei Ogawa: Writing – original draft, Investigation, Funding acquisition, Data curation, Conceptualization. **Akinobu Shibata:** Writing – review & editing, Supervision, Conceptualization.

Declaration of competing interest

The authors declare that they have no known competing financial interests or personal relationships that could have appeared to influence the work reported in this paper.

Acknowledgments

This work was financially supported by JSPS KAKENHI (Grant numbers: JP2 1K14045 and 24K17180). The authors are grateful to the technical staff in the Research Center for Hydrogen Industrial Use and Storage (HYDROGENIUS), Kyushu University, for their experimental support in hydrogen-charging (Section 2.2). Dr. Kaneaki Tsuzaki in NIMS is also greatly acknowledged for his helpful advisories in preparing this manuscript.

Supplementary materials

Supplementary material associated with this article can be found, in the online version, at doi:10.1016/j.actamat.2024.120659.

References

[1] D. Hull, D.J. Bacon, Introduction to Dislocations, 3rd ed., Butterworth-Heinemann, 2011. https://doi.org/10.1016/C2009-0-64358-0.
[2] D. Caillard, J.L. Martin, Thermally activated mechanisms in crystal plasticity, 1st ed., Pergamon, 2003.
[3] A.G. Evans, R.D. Rawlings, The thermally activated deformation of crystalline materials, Phys. Status Solidi 34 (1969) 9–31, https://doi.org/10.1002/pssb.19690340102.
[4] F. Guiu, P.L. Pratt, Stress relaxation and the plastic deformation of solids, Phys. Status Solidi 6 (1964) 111–120, https://doi.org/10.1002/pssb.19640060108.
[5] J.L. Martin, B. Lo Piccolo, T. Kruml, J. Bonneville, Characterization of thermally activated dislocation mechanisms using transient tests, Mater. Sci. Eng. A 322 (2002) 118–125, https://doi.org/10.1016/S0921-5093(01)01124-8.
[6] P. Spätig, J. Bonneville, J.-L. Martin, A new method for activation volume measurements: application to Ni3(Al,Hf), Mater. Sci. Eng. A 167 (1993) 73–79, https://doi.org/10.1016/0921-5093(93)90339-G.
[7] P. Groh, R. Conte, Stress relaxation and creep in α-iron filamentary single crystals at low temperature, Acta Metall. 19 (1971) 895–902, https://doi.org/10.1016/0001-6160(71)90082-4.
[8] G. Laplanche, J. Bonneville, C. Varvenne, W.A. Curtin, E.P. George, Thermal activation parameters of plastic flow reveal deformation mechanisms in the CrMnFeCoNi high-entropy alloy, Acta Mater. 143 (2018) 257–264, https://doi.org/10.1016/j.actamat.2017.10.014.
[9] E. Sirois, H.K. Birnbaum, Effects of hydrogen and carbon on thermally activated deformation in nickel, Acta Metall. et Mater. 40 (1992) 1377–1385, https://doi.org/10.1016/0956-7151(92)90438-K.
[10] R.A. Mulford, Analysis of strengthening mechanisms in alloys by means of thermal-activation theory, Acta Metall. 27 (1979) 1115–1124, https://doi.org/10.1016/0001-6160(79)90129-9.
[11] S. Mishra, V.K. Beura, A. Singh, M. Yadava, Effect of obstacle strength and spacing on the slope of Haasen plot, Mater. Sci. Technol. 35 (2019) 403–408, https://doi.org/10.1080/02670836.2019.1567043.
[12] A. Oehlert, A. Atrens, Room temperature creep of high strength steels, Acta Metall. Mater. 42 (1994) 1493–1508, https://doi.org/10.1016/0956-7151(94)90360-3.
[13] Z.S. Basinski, R.A. Foxall, R. Pascual, Stress equivalence of solution hardening, Scripta Metall. 6 (1972) 807–814, https://doi.org/10.1016/0036-9748(72)90052-X.
[14] U.F. Kocks, Kinetics of solution hardening, Metall. Trans. A 16 (1985) 2109–2129, https://doi.org/10.1007/BF02670415.
[15] W.A. Curtin, New interpretation of the Haasen plot for solute-strengthened alloys, Scr. Mater. 63 (2010) 917–920, https://doi.org/10.1016/j.scriptamat.2010.07.003.
[16] M.L.G. Byrnes, M. Grujicic, W.S. Owen, Nitrogen strengthening of a stable austenitic stainless steel, Acta Metall. 35 (1987) 1853–1862, https://doi.org/10.1016/0001-6160(87)90131-3.
[17] L.H. de Almeida, I. Le May, P.R.O. Emygdio, Mechanistic modeling of dynamic strain aging in austenitic stainless steels, Mater. Charact. 41 (1998) 137–150, https://doi.org/10.1016/S1044-5803(98)00031-X.
[18] J. Mola, G. Luan, Q. Huang, C. Ullrich, O. Volkova, Y. Estrin, Dynamic strain aging mechanisms in a metastable austenitic stainless steel, Acta Mater. 212 (2021) 116888, https://doi.org/10.1016/j.actamat.2021.116888.
[19] U.F. Kocks, R.E. Cook, R.A. Mulford, Strain aging and strain hardening in Ni-C alloys, Acta Metall. 33 (1985) 623–638, https://doi.org/10.1016/0001-6160(85)90026-4.
[20] N. Ohkubo, K. Miyakusu, Y. Uematsu, H. Kimura, Effect of alloying elements on the mechanical properties of the stable austenitic stainless steel, ISIJ Int. 34 (1994) 764–772, https://doi.org/10.2355/isijinternational.34.764.
[21] J. Raviers, G. Slavens, Strengthening Characteristics of Nitrogen-Alloyed 201 Stainless Steel, J. Mater. Eng. Perform. 4 (1995) 697–708, https://doi.org/10.1007/BF02646446.
[22] H.M. Ledbetter, M.W. Austin, Dilation of an fcc Fe–Cr–Ni alloy by interstitial carbon and nitrogen, Mater. Sci. Technol. 3 (1987) 101–104, https://doi.org/10.1179/mst.1987.3.2.101.
[23] E.N. Epperly, R.B. Sills, Transient solute drag and strain aging of dislocations, Acta Mater. 193 (2020) 182–190, https://doi.org/10.1016/j.actamat.2020.03.031.

[24] D.G. Ulmer, C.J. Altstetter, Phase relations in the hydrogen-austenite system, Acta Metall. Et Mater. 41 (1993) 2235–2241, https://doi.org/10.1016/0956-7151(93)90393-7.
[25] X.W. Zhou, C. Nowak, R.S. Skelton, M.E. Foster, J.A. Ronevich, C. San Marchi, R. B. Sills, An Fe–Ni–Cr–H interatomic potential and predictions of hydrogen-affected stacking fault energies in austenitic stainless steels, Int. J. Hydrogen. Energy 47 (2022) 651–665, https://doi.org/10.1016/j.ijhydene.2021.09.261.
[26] J. Moriyama, O. Takakuwa, M. Yamaguchi, Y. Ogawa, K. Tsuzaki, The contribution of Cr and Ni to hydrogen absorption energy in Fe-Cr-Ni austenitic systems: a first-principles study, Comput. Mater. Sci. 232 (2024) 112650, https://doi.org/10.1016/j.commatsci.2023.112650.
[27] Z. Hua, B. An, T. Iijima, C. Gu, J. Zheng, The finding of crystallographic orientation dependence of hydrogen diffusion in austenitic stainless steel by scanning Kelvin probe force microscopy, Scr. Mater. 131 (2017) 47–50, https://doi.org/10.1016/j.scriptamat.2017.01.003.
[28] T. Perng, C.J. Altstetter, Effects of deformation on hydrogen permeation in austenitic stainless steels, Acta Metall. 34 (1986) 1771–1781, https://doi.org/10.1016/0001-6160(86)90123-9.
[29] I.M. Robertson, The effect of hydrogen on dislocation dynamics, Eng. Fract. Mech. 68 (2001) 671–692, https://doi.org/10.1016/S0013-7944(01)00011-X.
[30] C.W. Tien, C.J. Altstetter, Hydrogen-enhanced plasticity of 310S stainless steel, Mater. Chem. Phys. 35 (1993) 58–63, https://doi.org/10.1016/0254-0584(93)90177-N.
[31] D.P. Abraham, C.J. Altstetter, Hydrogen-enhanced localization of plasticity in an austenitic stainless steel, Metall. Mater. Trans. A 26 (1995) 2859–2871, https://doi.org/10.1007/BF02669644.
[32] T. Boniszewski, G.C. Smith, The influence of hydrogen on the plastic deformation ductility, and fracture of nickel in tension, Acta Metall. 11 (1963) 165–178, https://doi.org/10.1016/0001-6160(63)90209-8.
[33] J.S. Blakemore, The portevin-le chatelier effect in hydrogenated nickel alloys, Metall. Mater. Trans. 1 (1970) 151–156, https://doi.org/10.1007/BF02819255.
[34] M. Koyama, K. Ichii, K. Tsuzaki, Strain rate and temperature effects on hydrogen embrittlement of stable and metastable high-entropy alloys, Phys. Mesomech. 25 (2022) 385–392, https://doi.org/10.1134/S1029959922050010.
[35] D.P. Abraham, C.J. Altstetter, The effect of hydrogen on the yield and flow stress of an austenitic stainless steel, Metall. Mater. Trans. A 26 (1995) 2849–2858, https://doi.org/10.1007/BF02669643.
[36] Y. Ogawa, O. Takakuwa, K. Tsuzaki, Solid-solution hardening by hydrogen in Fe–Cr–Ni-based austenitic steel: temperature and strain rate effects, Mater. Sci. Eng. A (2023) 145281, https://doi.org/10.1016/j.msea.2023.145281.
[37] K. Wada, J. Yamabe, Y. Ogawa, O. Takakuwa, T. Iijima, H. Matsunaga, Comparative study of hydrogen-induced intergranular fracture behavior in Ni and Cu–Ni alloy at ambient and cryogenic temperatures, Mater. Sci. Eng. A 766 (2019) 138349, https://doi.org/10.1016/j.msea.2019.138349.
[38] S.K. Lawrence, Y. Yagodzinskyy, H. Hänninen, E. Korhonen, F. Tuomisto, Z. D. Harris, B.P. Somerday, Effects of grain size and deformation temperature on hydrogen-enhanced vacancy formation in Ni alloys, Acta Mater. 128 (2017) 218–226, https://doi.org/10.1016/j.actamat.2017.02.016.
[39] G. Girardin, D. Delafosse, Measurement of the saturated dislocation pinning force in hydrogenated nickel and nickel base alloys, Scr. Mater. 51 (2004) 1177–1181, https://doi.org/10.1016/j.scriptamat.2004.07.012.
[40] J.S. Blakemore, The Portevin-Le Chatelier Effect in hydrogenated nickel, Metall. Trans. 1 (1970) 145–149, https://doi.org/10.1007/BF02819254.
[41] B.A. Wilcox, G.C. Smith, The Portevin-Le Chatelier effect in hydrogen charged nickel, Acta Metall. 12 (1964) 371–376, https://doi.org/10.1016/0001-6160(64)90006-9.
[42] K. Wada, J. Yamabe, H. Matsunaga, Mechanism of hydrogen-induced hardening in pure nickel and in a copper–nickel alloy analyzed by micro Vickers hardness testing, Mater. Sci. Eng. A 805 (2021) 140580, https://doi.org/10.1016/j.msea.2020.140580.
[43] K. Ichii, M. Koyama, C.C. Tasan, K. Tsuzaki, Comparative study of hydrogen embrittlement in stable and metastable high-entropy alloys, Scr. Mater. 150 (2018) 74–77, https://doi.org/10.1016/j.scriptamat.2018.03.003.
[44] O. Takakuwa, Y. Mano, H. Soyama, Increase in the local yield stress near surface of austenitic stainless steel due to invasion by hydrogen, Int. J. Hydrogen. Energy 39 (2014) 6095–6103, https://doi.org/10.1016/j.ijhydene.2014.01.190.
[45] C.San Marchi, B.P. Somerday, X. Tang, G.H. Schiroky, Effects of alloy composition and strain hardening on tensile fracture of hydrogen-precharged type 316 stainless steels, Int. J. Hydrogen. Energy 33 (2008) 889–904, https://doi.org/10.1016/j.ijhydene.2007.10.046.
[46] Y. Murakami, T. Kanezaki, Y. Mine, Hydrogen effect against hydrogen embrittlement, Metall. Mater. Trans. A 41 (2010) 2548–2562, https://doi.org/10.1007/s11661-010-0275-6.
[47] P.J. Ferreira, I.M. Robertson, H.K. Birnbaum, Hydrogen effects on the interaction between dislocations, Acta Mater. 46 (1998) 1749–1757, https://doi.org/10.1016/S1359-6454(97)00349-2.
[48] T. Matsumoto, J. Eastman, H.K. Birnbaum, Direct observations of enhanced dislocation mobility due to hydrogen, Scripta Metall. 15 (1981) 1033–1037, https://doi.org/10.1016/0036-9748(81)90249-0.
[49] T. Tabata, H.K. Birnbaum, Direct observations of the effect of hydrogen on the behavior of dislocations in iron, Scripta Metall. 17 (1983) 947–950, https://doi.org/10.1016/0036-9748(83)90268-5.
[50] J. Song, W.A. Curtin, Mechanisms of hydrogen-enhanced localized plasticity: an atomistic study using α-Fe as a model system, Acta Mater. 68 (2014) 61–69, https://doi.org/10.1016/j.actamat.2014.01.008.
[51] R. Matsumoto, S.T. Oyinbo, M. Vijendran, S. Taketomi, Hydrogen effect on the mobility of edge dislocation in α-iron: a long-timescale molecular dynamics simulation, ISIJ Int. 62 (2022), https://doi.org/10.2355/isijinternational.ISIJINT-2022-311. ISIJINT-2022-311.
[52] Q. Sun, J. He, A. Nagao, Y. Ni, S. Wang, Hydrogen-prompted heterogeneous development of dislocation structure in Ni, Acta Mater. 246 (2023) 118660, https://doi.org/10.1016/j.actamat.2022.118660.
[53] G. Girardin, C. Huvier, D. Delafosse, X. Feaugas, Correlation between dislocation organization and slip bands: TEM and AFM investigations in hydrogen-containing nickel and nickel–chromium, Acta Mater. 91 (2015) 141–151, https://doi.org/10.1016/j.actamat.2015.03.016.
[54] K. Nibur, D. Bahr, B. Somerday, Hydrogen effects on dislocation activity in austenitic stainless steel, Acta Mater. 54 (2006) 2677–2684, https://doi.org/10.1016/j.actamat.2006.02.007.
[55] H.K. Birnbaum, P. Sofronis, Hydrogen-enhanced localized plasticity—A mechanism for hydrogen-related fracture, Mater. Sci. Eng. A 176 (1994) 191–202, https://doi.org/10.1016/0921-5093(94)90975-X.
[56] H.K. Birnbaum, Hydrogen effects on deformation — Relation between dislocation behavior and the macroscopic stress-strain behavior, Scripta Metall. et Mater. 31 (1994) 149–153, https://doi.org/10.1016/0956-716X(94)90166-X.
[57] I. Aubert, J.-M. Olive, N. Saintier, The effect of internal hydrogen on surface slip localisation on polycrystalline AISI 316L stainless steel, Mater. Sci. Eng. A 527 (2010) 5858–5866, https://doi.org/10.1016/j.msea.2010.05.062.
[58] F.D. León-Cázares, X. Zhou, B. Kagay, J.D. Sugar, C. Alleman, J. Ronevich, C. San Marchi, Hydrogen effects on the deformation and slip localization in a single crystal austenitic stainless steel, Int. J. Plast. 180 (2024) 104074, https://doi.org/10.1016/j.ijplas.2024.104074.
[59] Y. Ogawa, M. Tanaka, T. Fujita, A. Shibata, Thermally activated dislocation motion in hydrogen-alloyed Fe–Cr–Ni austenitic steel revisited via Haasen plot, Int. J. Hydrogen. Energy 74 (2024) 170–182, https://doi.org/10.1016/j.ijhydene.2024.06.113.
[60] Y. Ogawa, T. Fujita, Solid solution-hardening by hydrogen in Fe–Cr–Ni-based austenitic steel studied by strain rate sensitivity measurement: contributions of effective stress and solute drag, Mater. Sci. Eng. A 911 (2024) 146941, https://doi.org/10.1016/j.msea.2024.146941.
[61] T. Zirkle, L. Costello, D.L. McDowell, Crystal plasticity modeling of hydrogen and hydrogen-related defects in initial yield and plastic flow of single-crystal stainless steel 316L, Metall. Mater. Trans. A 52 (2021) 3961–3977. https://doi.org/10.1007/s11661-021-06357-8.
[62] G.M. Castelluccio, C.B. Geller, D.L. McDowell, A rationale for modeling hydrogen effects on plastic deformation across scales in FCC metals, Int. J. Plast. 111 (2018) 72–84, https://doi.org/10.1016/j.ijplas.2018.07.009.
[63] E. Krempl, An experimental study of room-temperature rate-sensitivity, creep and relaxation of AISI type 304 stainless steel, J. Mech. Phys. Solids. 27 (1979) 363–375, https://doi.org/10.1016/0022-5096(79)90020-6.
[64] D. Kujawski, V. Kallianpur, E. Krempl, An experimental study of uniaxial creep, cyclic creep and relaxation of aisi type 304 stainless steel at room temperature, J. Mech. Phys. Solids. 28 (1980) 129–148, https://doi.org/10.1016/0022-5096(80)90018-6.
[65] R.P. Reed, R.P. Walsh, Low-temperature creep of austenitic stainless steels, J. Phys. Conf. Ser. 897 (2017) 012002, https://doi.org/10.1088/1742-6596/897/1/012002.
[66] Y. Hong, C. Zhou, Y. Zheng, J. Zheng, L. Zhang, X. Chen, Hydrogen effect on nanoindentation creep of austenitic stainless steel: a comparative study between primary creep stage and steady-state creep stage, Int. J. Hydrogen. Energy 44 (2019) 22576–22583, https://doi.org/10.1016/j.ijhydene.2019.01.023.
[67] Y. Mine, T. Kimoto, Hydrogen uptake in austenitic stainless steels by exposure to gaseous hydrogen and its effect on tensile deformation, Corros. Sci. 53 (2011) 2619–2629, https://doi.org/10.1016/j.corsci.2011.04.022.
[68] Y. Ogawa, H. Hosoi, K. Tsuzaki, T. Redarce, O. Takakuwa, H. Matsunaga, Hydrogen, as an alloying element, enables a greater strength-ductility balance in an Fe-Cr-Ni-based, stable austenitic stainless steel, Acta Mater. 199 (2020) 181–192, https://doi.org/10.1016/j.actamat.2020.08.024.
[69] H. Nishida, Y. Ogawa, K. Tsuzaki, Chemical composition dependence of the strength and ductility enhancement by solute hydrogen in Fe–Cr–Ni-based austenitic alloys, Mater. Sci. Eng. A 836 (2022) 142681, https://doi.org/10.1016/j.msea.2022.142681.
[70] M. Tendo, T. Takeshita, T. Nakazawa, H. Kimura, H. Abo, Room temperature creep behavior of stainless steels, Tetsu-to-Hagane 79 (1993) 98–104, https://doi.org/10.2355/tetsutohagane1955.79.1_98.
[71] Y. Estrin, H. Mecking, A unified phenomenological description of work hardening and creep based on one-parameter models, Acta Metall. 32 (1984) 57–70, https://doi.org/10.1016/0001-6160(84)90202-5.
[72] T. Kruml, O. Coddet, J.L. Martin, The investigation of internal stress fields by stress reduction experiments, Mater. Sci. Eng. A 387–389 (2004) 72–75, https://doi.org/10.1016/j.msea.2004.01.066.
[73] R. Madec, B. Devincre, L.P. Kubin, From Dislocation Junctions to Forest Hardening, Phys. Rev. Lett. 89 (2002) 255508, https://doi.org/10.1103/PhysRevLett.89.255508.
[74] G. Saada, Sur le durcissement dû à la recombinaison des dislocations, Acta Metall. 8 (1960) 841–847, https://doi.org/10.1016/0001-6160(60)90150-4.
[75] R.B. Sills, N. Bertin, A. Aghaei, W. Cai, Dislocation networks and the microstructural origin of strain hardening, Phys. Rev. Lett. 121 (2018) 085501, https://doi.org/10.1103/PhysRevLett.121.085501.

[76] T. Hasegawa, T. Yakou, U.F. Kocks, Forward and reverse rearrangements of dislocations in tangled walls, Mater. Sci. Eng. 81 (1986) 189–199, https://doi.org/10.1016/0025-5416(86)90262-4.
[77] H. Mughrabi, Dislocation wall and cell structures and long-range internal stresses in deformed metal crystals, Acta Metall. 31 (1983) 1367–1379, https://doi.org/10.1016/0001-6160(83)90007-X.
[78] X. Feaugas, On the origin of the tensile flow stress in the stainless steel AISI 316L at 300 K: back stress and effective stress, Acta Mater. 47 (1999) 3617–3632, https://doi.org/10.1016/S1359-6454(99)00222-0.
[79] J.C.M. Li, Dislocation dynamics in deformation and recovery, Can. J. Phys. 45 (1967) 493–509, https://doi.org/10.1139/p67-043.
[80] S.R. MacEwen, O.A. Kupcis, B. Ramaswami, An investigation of an incremental unloading technique for estimating internal stresses, Scripta Metall. 3 (1969) 441–448, https://doi.org/10.1016/0036-9748(69)90128-8.
[81] T. Kruml, O. Coddet, J.L. Martin, About the determination of the thermal and athermal stress components from stress-relaxation experiments, Acta Mater. 56 (2008) 333–340, https://doi.org/10.1016/j.actamat.2007.09.027.
[82] H. Mecking, U.F. Kocks, Kinetics of flow and strain-hardening, Acta Metall. 29 (1981) 1865–1875, https://doi.org/10.1016/0001-6160(81)90112-7.
[83] U.F. Kocks, H. Mecking, Physics and phenomenology of strain hardening: the FCC case, Prog. Mater. Sci. 48 (2003) 171–273, https://doi.org/10.1016/S0079-6425(02)00003-8.
[84] O.H. Wyatt, Transient creep in pure metals, Nature 167 (1951), https://doi.org/10.1038/167866a0, 866–866.
[85] A.H. Cottrell, The time laws of creep, J. Mech. Phys. Solids. 1 (1952) 53–63, https://doi.org/10.1016/0022-5096(52)90006-9.
[86] M. Tendo, T. Takeshita, T. Nakazawa, Relationship between Room temperature creep behavior and yield strength in austenitic stainless steels, Tetsu-to-Hagane 80 (1994) 149–154, https://doi.org/10.2355/tetsutohagane1955.80.2_149.
[87] Y. Ogawa, H. Nishida, O. Takakuwa, K. Tsuzaki, Hydrogen-enhanced deformation twinning in Fe-Cr-Ni-based austenitic steel characterized by in-situ EBSD observation, Mater. Today Commun. 34 (2023) 105433, https://doi.org/10.1016/j.mtcomm.2023.105433.
[88] Y. Ogawa, Temperature-sensitive ductilization in hydrogen-alloyed Fe-Cr-Ni austenitic steel by enhanced deformation twinning, Scr. Mater. 238 (2024) 115760, https://doi.org/10.1016/j.scriptamat.2023.115760.
[89] Y. Estrin, L.P. Kubin, Local strain hardening and nonuniformity of plastic deformation, Acta Metallur. 34 (1986) 2455–2464, https://doi.org/10.1016/0001-6160(86)90148-3.
[90] J. Bonneville, B. Escaig, J.L. Martin, A study of cross-slip activation parameters in pure copper, Acta Metallur. 36 (1988) 1989–2002, https://doi.org/10.1016/0001-6160(88)90301-X.
[91] P.S. Follansbee, U.F. Kocks, A constitutive description of the deformation of copper based on the use of the mechanical threshold stress as an internal state variable, Acta Metallur. 36 (1988) 81–93, https://doi.org/10.1016/0001-6160(88)90030-2.
[92] T.H. Alden, Theory of mobile dislocation density: application to the deformation of 304 stainless steel, Metallurg.Trans. A 18 (1987) 51–62, https://doi.org/10.1007/BF02646221.
[93] R. Kirchheim, Reducing grain boundary, dislocation line and vacancy formation energies by solute segregation. I. Theoretical background, Acta Mater. 55 (2007) 5129–5138, https://doi.org/10.1016/j.actamat.2007.05.047.
[94] J. Friedel, Dislocations, 1st ed, Pergamon Press, 1964.
[95] Y. Dong, W.A. Curtin, Thermally activated plastic flow in the presence of multiple obstacle types, Model. Simul. Mat. Sci. Eng. 20 (2012) 075006, https://doi.org/10.1088/0965-0393/20/7/075006.
[96] U.F. Kocks, A.S. Argon, M.F. Ashby, Thermodynamics and kinetics of slip, Prog. Mater. Sci. 19 (1975) 110–170, https://doi.org/10.1016/0079-6425(75)90008-0.
[97] U.F. Kocks, Superposition of alloy hardening, strain hardening, and dynamic recovery. Strength of Metals and Alloys, Elsevier, 1979, pp. 1661–1680, https://doi.org/10.1016/B978-1-4832-8412-5.50250-2.